J. Appl. Comput. Mech., xx(x) (2025) 1-11
DOI: 10.22055/jacm.2025.48733.5459

ISSN: 2383-4536
jacm.scu.ac.ir

Shahid Chamran University of Ahvaz

Journal of Applied and Computational Mechanics

Research Paper

Proper Orthogonal Decomposition Analysis of Turbulent Energy Spectra within a Lagrangian Particle Tracking Framework

Reza Hassanian

Faculty of Industrial Engineering, Mechanical Engineering and Computer Science, University of Iceland, Reykjavik, 102, Iceland, Email: seh@hi.is

Received September 04 2025; Revised December 02 2025; Accepted for publication December 05 2025.
Corresponding author: R. Hassanian (seh@hi.is)

Abstract. This paper proposes an approach that applies Proper Orthogonal Decomposition (POD) analysis to experimental data obtained using the Lagrangian Particle Tracking (LPT) technique from the original experimental work [1]. Based on the experiment description, it was conducted under two flow conditions: (a) nearly Homogeneous Isotropic Turbulence (HIT) with a Taylor microscale Reynolds number in the range $100 < Re_\lambda < 120$, and (b) initially HIT flow subjected to strain deformation in the Y-direction with a mean strain rate of 8 s^{-1}. The LPT-based POD analysis, using individual particle velocity data, yields several significant findings. Constructing the data matrix from the velocity fields of individual particles introduces a novel aspect to the analysis. POD is employed to uncover the effects of strain deformation on the energy spectra in contrast to the HIT flow. The energy spectra of flows with varying turbulence intensities and subjected to strain deformation illustrate how these factors influence the overall energy distribution. Furthermore, spectral analysis of turbulent structures shows that power-law behavior in the energy spectrum can be captured by POD analysis. Strain deformation alters the energy contributions of the POD modes, leading to a significantly increased concentration of energy in the first few dominant modes. The LPT-based POD exhibits significantly low computational cost per realization.

Keywords: Turbulent flow, Proper orthogonal decomposition, Energy spectra, Coherent structures, Computation.

1. Introduction

Turbulent flow is a complex phenomenon that occurs in most fluid dynamics scenarios [2], and it remains not fully understood [3]. The governing equations for turbulence are nonlinear, making their solution at high Reynolds numbers extremely challenging, even for simple geometries [4]. Turbulence exhibits a vast range of degrees of freedom across both spatial and temporal scales, a characteristic consistently supported by experimental evidence [4, 5]. There are two primary analytical approaches to studying turbulent flow: statistical and deterministic [4]. Observations reveal that turbulent flow is highly sensitive to perturbations that inevitably arise from initial conditions, boundary conditions, and material properties [6]. These findings help reconcile the apparent contradiction between the inherently random nature of turbulence and the deterministic foundation of the Navier-Stokes equations [6].

The statistical approach to turbulence analysis traces back to Reynolds' work in 1894 [7]. In contrast, the deterministic approach appears to have originated from nonlinear stability analysis and amplitude equations. Lumley et al. suggested that L. D. Landau and J. T. Stuart should be credited with pioneering an analytical, non-statistical perspective [4]. However, the statistical approach has limitations, and it primarily benefits in studying transition and perturbation states. Its primary drawback is its reliance on average quantities, which leads to closure problems that often require empirical data and complex renormalization-group theories to address [4].

Computational Fluid Dynamics (CFD) represents the third major approach to studying fluid flow [8]. Modern numerical analysis in this field traces its origins to a seminal paper by Courant et al. [9], which introduced the stability condition for the solution of hyperbolic partial differential equations. The first numerical solution for flow past a cylinder was published by Thom in 1933 [10].

Unlike traditional analytical methods, which derive solutions through logical, step-by-step deductions, CFD simulations provide minimal theoretical insight into the solutions they produce. Instead, CFD resembles an experimental approach, relying on numerical approximations rather than purely analytical derivations. Nevertheless, its significance remains high due to the vast amount of data it generates [4]. Studying turbulent flow requires both predictive capabilities and a deep understanding of its underlying processes [11]. Each of the aforementioned approaches aims to provide insight into turbulence and its inherent structures, yet each has its limitations. Both analytical and CFD methods depend on the physical nature of the problem. However, the applicability of analytical methods is constrained by uncertainties in initial and boundary conditions [6].

In CFD, turbulent flow simulations are categorized into three main approaches: Reynolds-averaged Navier-Stokes (RANS), Large Eddy Simulation (LES), and Direct Numerical Simulation (DNS) [12]. Among these, DNS provides the most accurate simulations but is also the most computationally expensive. LES offers a balance between accuracy and cost, being more precise than RANS but less cost-demanding than DNS. RANS, on the other hand, delivers an average solution at a significantly lower computational cost, making it the most widely used method in industrial applications [12]. Although computing power is advancing rapidly, even reaching the Exascale level [13], there are challenges in memory and computation that prevent the resolution of every CFD problem with complete accuracy, particularly for high-Reynolds-number flows and complex three-dimensional simulations. In recent years, Machine Learning (ML) has emerged and grown as a powerful tool for predicting turbulent flow using data obtained from experimental measurements or CFD simulations [14]. A Data-Driven Model (DDM) is an ML-based approach that uses turbulent flow data [15], leveraging its spatiotemporal features to construct a predictive model based on the chosen ML architecture [11]. This method enables the prediction of turbulent flow fields with varying degrees of accuracy, depending on the specific ML or Deep Learning (DL) model applied [16].

Proper Orthogonal Decomposition (POD) is a technique used to derive a basis for modal decomposition from a set of signals [17]. This method is particularly valuable due to its mathematical properties, which make it the optimal basis for many applications [18]. The significance of POD in turbulence research was first recognized by Lumley, who introduced it in 1967 and further elaborated on its applications in 1981 [4, 19]. Since then, it has become a fundamental tool for analyzing complex flow dynamics. Although POD may not encompass the broad scope of the previously mentioned approaches, it still provides valuable contributions, as outlined in the following [4]. POD allows the extraction of spatial and temporal structures from a turbulent field using predetermined criteria. It provides a rigorous mathematical framework for describing these structures, making it a powerful tool for analyzing and synthesizing data from experiments and simulations. Additionally, POD facilitates the construction of low-dimensional dynamical models derived from the Navier-Stokes equations to capture interactions among these essential structures [4]. The method is grounded in statistical principles and relies on data from experiments and simulations. Its strong analytical foundations offer a clear understanding of both its capabilities and limitations. Furthermore, the dominant coherent structures identified by POD can enhance ML models, thereby improving predictions of turbulent flow fields.

The standard POD is formulated based on spatial correlations and requires complete field data over all grid points. This approach is computationally intensive and generally impractical for large-scale DNS or LES datasets [20]. In contrast, the snapshot POD [20, 21] offers significantly improved computational efficiency by constructing correlations in the temporal domain rather than the spatial one. It employs Eulerian snapshots of flow variables recorded at fixed grid locations over time. Nevertheless, this method assumes sufficiently dense temporal sampling to capture all energetic modes and only resolves spatial structures through snapshot correlations, rendering temporal coherence implicit [20, 21]. The Spectral POD [20, 22], formulated in the frequency domain, utilizes time-resolved grid data and is particularly suited for stationary, time-resolved turbulent flows. However, it entails a higher computational cost compared to the Snapshot POD [20, 22].

The motivation of this study is to employ Proper Orthogonal Decomposition (POD) to analyze experimental data of turbulent flow obtained through the Lagrangian Particle Tracking (LPT) technique. The dataset consists of particle trajectories recorded over a defined time interval, representing the flow from a Lagrangian perspective that captures both temporal and spatial characteristics. Consequently, the amount of data is comparable to that used in snapshot POD and standard POD analyses applied to full-field measurements. Moreover, the velocity field, which embodies key flow characteristics, exhibits strong correlations with both temporal and spatial features. The proposed approach offers computational efficiency comparable to that of direct and snapshot POD algorithms while retaining the ability to capture approximately 90% of the turbulent kinetic energy. Therefore, the advantages of this method highlight the potential of integrating POD with LPT for the analysis of both experimental and numerical turbulent flow dataset.

Additionally, the study aims to illustrate the effect of imposed strain on the dominant modes identified through POD analysis. Furthermore, it investigates the energy spectrum of the POD modes, the existence of a power-law behavior, and how it is influenced by the presence of strain.

The novelty of this study lies in its use of the POD approach on data from LPT and in defining the matrix set up for turbulent flow fields. In fluid dynamics, LPT is also known as particle tracking velocity (PTV). However, in this study, we will consistently refer to the measurement technique as LPT. Furthermore, the study uses data from a unique experiment conducted under two distinct conditions: one with purely turbulent flow initialized in a nearly homogeneous and isotropic state, and another with strain deformation, also initialized in a nearly homogeneous and isotropic state.

The results of the POD analysis reveal remarkable insights into how strain affects the coherent structures and dominant POD modes. Additionally, the energy distribution across modes demonstrates a significant influence of strain, yielding superior results for turbulent flow under deformation—an observation relevant to various artificial and natural applications.

Hence, this paper is structured as follows: Section 2 describes the experimental data and measured data, while Section 3 presents the fundamentals and theory of POD applications. Section 4 outlines the approach for applying POD to LPT data, Section 5 discusses the results, and Section 6 provides the conclusion.

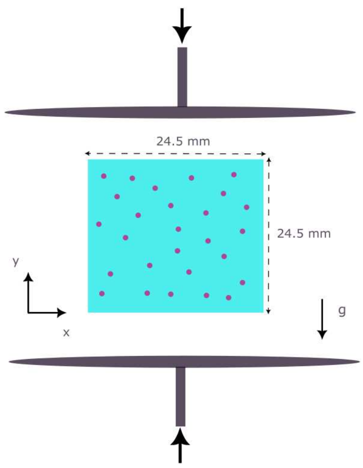

Fig. 1. A schematic of the experimental setup, with the measurement area located in the center of the tank. The turbulent tank dimension is 60 cm × 60 cm × 60 cm. Two circular cylinders with linear actuators moving toward the center to generate the strain deformation. The flow is water and seeded with tracer particles.

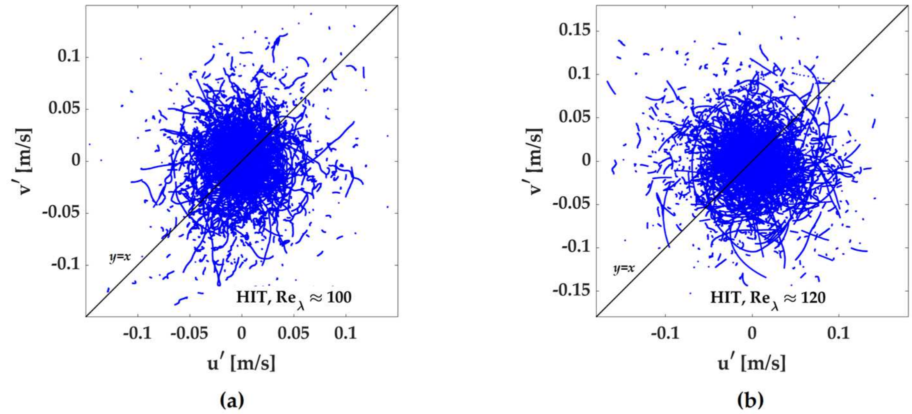

Fig. 2. Velocity fluctuation samples using scatter plots in isotropic turbulent fields from two turbulent flows: (a) $Re_\lambda \approx 100$, (b) $Re_\lambda \approx 120$. Each dot marks a (u',v') pair at a specific sample time, with multiple sample times depicted in each panel. In the isotropic case, the distribution forms a symmetric cloud of points, indicating that the average value of $u'v'$ is zero.

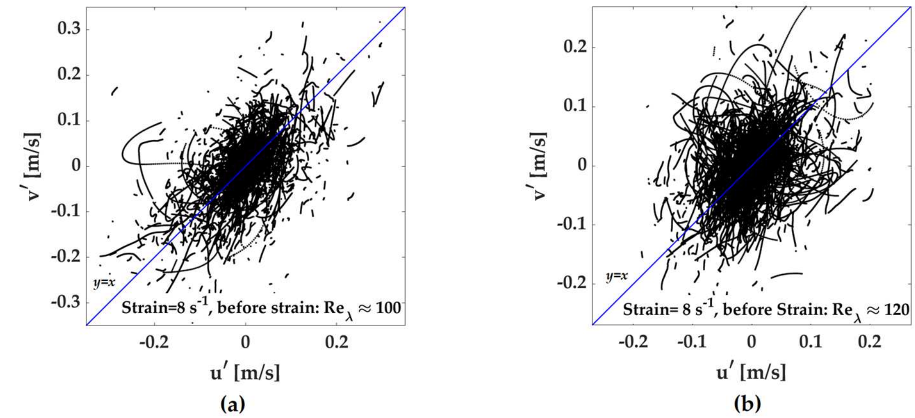

Fig. 3. Velocity fluctuation samples using scatter plots in anisotropic turbulent fields from two turbulent flows under strain deformation: (a) mean strain rate is 8 s^{-1} and with $Re_\lambda \approx 100$ before strain deformation, (b) mean strain rate is 8 s^{-1} and with $Re_\lambda \approx 120$ before strain deformation. In this anisotropic case, the data clustering around the line $u' = v'$, and this indicates a positive correlation of u and v, which is $u'v' \geq 0$.

2. Experimental Data

The dataset originates from turbulent flow experiments conducted in a controlled laboratory environment, with comprehensive details available in the original study [1]. The flow exhibits a Taylor microscale within the range of $100 < Re_\lambda < 120$. It underwent strain-induced deformation at a mean rate of 8 s^{-1} along the Y-direction. The experiment took place under the influence of gravity, simulating real-world turbulent flow. The generated turbulent flow has a nearly homogeneous isotropic initial condition. Figure 1 shows a schematic of the experimental setup, including the location of the measurement area and the motion of the two circular cylinders moving toward the center of the turbulent tank to generate strain deformation. The measurement area is positioned sufficiently far from the tank walls to minimize wall and boundary layer effects [1]. Figure 2 shows the isotropic flow condition for the measured data from the experiment with two different turbulence intensities of $Re_\lambda \approx 100$ and $Re_\lambda \approx 120$.

To capture flow characteristics, tracer particles with median diameters of 8–10 μm and a specific gravity of 1.1 g/cm^3 (hollow glass) were introduced into the flow. Their motion was monitored using an LPT technique, following the approach developed by Ouellette et al. [23]. A high-speed camera, operating in a 2D configuration, documented the trajectories of these tracer particles.

The original study evaluated the tracer particles' behavior using the Stokes number (St) to confirm that their motion followed the flow streamlines. The Stokes number is defined as $St = \tau_p/\tau_\eta$ where τ_p is the particle relaxation time, and τ_η is the Kolmogorov time scale [1, 6]. As it is described in the original work [1], the Particle Image Velocimetry (PIV) measurement is applied to extract the flow characteristics, which is conducted the experiment with a higher number of particles (dense seeded flow) before applying the strain, which is a nearly stationary, homogeneous turbulent flow, and data are taken on a grid obtained from PIV measurements [1]. In the inertial subrange, the compensated structure functions are nearly constant, allowing us to determine the dissipation rate ε in the flow; here we use r, the separation between 60η and $L/6$, as suggested by Pope [6], η is the Kolmogorov length scale, r is the separation, and L is the integral length scale. Kolmogorov scale based on PIV, calculated as $\tau_\eta = (\nu/\varepsilon)^{1/2}$ where ν is the kinematic viscosity of the fluid, which is water in this experiment, and ε the energy dissipation rate is evaluated via the second-order longitudinal velocity structure function [1, 6]. The relaxation time is calculated as $\tau_p = \rho_p {d_p}^2/18\mu$ where ρ_p is particle density, d_p is the spherical particle diameter, and μ is the dynamic fluid viscosity [1]. The St number serves as an indicator, where $St \ll 1$ ensures that a particle's trajectory closely follows the fluid motion. For the seeded particles, the St number was reported to be within the range of 0.00632–0.01807 [1].

The collected data encompassed velocity components in the X and Y directions, positional coordinates (x, y), and corresponding timestamps t for each recorded instant. Measurements were captured at 10,000 frames per second (10 kHz). This exceptionally high temporal resolution (0.1–0.2 ms) is much smaller than the Kolmogorov timescale, τ_η (35–99 ms) [1], corresponding to the smallest eddies in the flow, thereby allowing the characteristics of the energy dissipation range to be fully resolved. From a Lagrangian perspective, the motion of a fluid particle is defined by [6]:

$$x_i = x_i(t, X_0), \qquad\qquad i = 1,2,3 \tag{1}$$

$$U_i = U_i(t, x_1(t, X_0), x_2(t, X_0), x_3(t, X_0)) \tag{2}$$

where the location and velocity of a fluid particle in 3D space are represented by Eqs. (1) and (2), respectively. Here, x denotes position, U signifies velocity, X_0 denote the initial condition, t corresponds to time, and i indicates the vector component. The initially homogeneous isotropic flow underwent strain in the Y-direction, and Fig. 3 illustrates the resulting anisotropic turbulent fields. The Reynolds stress anisotropy tensor is correlated with the strain rate, and the visualizations in Figs. 2 and 3 illustrate this relationship and its effects.

This paper uses laboratory-measured data in a novel approach for POD analysis of turbulent flow based on LPT data. This POD implementation computes only the data from tracked particles in the flow, allowing the study of coherent structures without expending computational resources on the entire domain grid.

3. Theory

This section explains the fundamental concept of the POD applied to LPT data. POD is a data-driven technique for extracting dominant modes or patterns from complex systems by reducing high-dimensional data to a low-dimensional representation [24, 25].

3.1. POD

The aim is to obtain an approximate representation of the function $z(x,t)$ within a specified domain by a finite summation in which the spatial and temporal variables are separated, therefore [26]:

$$z(x,t) \approx \sum_{k=1}^{M} a_k(t)\varphi_k(x)\,, \tag{3}$$

with the reasonable assumption that the approximation converges to the exact solution as M tends to infinity, except potentially on a set of measure zero. Although Eq. (3) does not intrinsically differentiate between t and x, it is customary to interpret x as a spatial coordinate (possibly vector-valued) and t as a temporal coordinate [27].

The formulation presented in Eq. (3) is not uniquely defined. The POD method emphasizes a particular choice of basis functions, $\varphi_k(x)$. If an orthonormal set of basis functions has been selected, i.e.,

$$\int_x \varphi_{k_1}(x)\varphi_{k_2}(x)dx = \begin{cases}1, & if\ k_1 = k_2\\ 0, & otherwise\end{cases}, \tag{4}$$

then,

$$a_k(t) = \int_x z(x,t)\varphi_k(x)dx\,, \tag{5}$$

i.e., when using an orthonormal set of basis functions, the computation of the coefficient function $a_k(t)$ relies solely on $\varphi_k(x)$ and remains independent of the other φ's [27].

The selection criterion for $\varphi_k(x)$ is based on orthonormality. Furthermore, although it is always possible to achieve an approximation with any desired accuracy in Eq. (5) by selecting a sufficiently large M, it is preferable to choose $\varphi_k(x)$ in a manner that ensures the best possible approximation for each M in a least-squares sense [28]. The goal is to identify, once and for all, a sequence of orthonormal functions $\varphi_k(x)$ such that the first two functions provide the optimal two-term approximation, the first seven yield the best possible seven-term approximation, and so forth. These specifically ordered orthonormal functions are referred to as the proper orthogonal modes for the function $z(x,t)$. With these functions, the representation in Eq. (5) is known as the POD of $z(x,t)$ [29].

3.2. POD data matrix in Lagrangian viewpoint

This paper uses data from the LPT method that tracks individual particles in a turbulent flow. Figure 4 illustrates the tracked particles' motion from the LPT measurement as the determined area. The measurement area is a square 24.5 *mm* × 24.5 *mm* located in the center of the turbulent tank and far enough from the tank wall. The specifics of LPT as a measurement technique are beyond the scope of this study, and detailed information about the experiment can be found in the original work [1].

Here, POD is applied to analyze the velocity fields of HIT and strained turbulent flows, each examined in distinct configurations. Consequently, the measurement data consists of velocity vectors corresponding to each particle in the experiment:

$$u_j^p = u_j^p(t_b), \qquad j = 1, \dots, n, \qquad b = 1, \dots, m, \tag{6}$$

u_j^p represents the measured velocity component of a particle, where $u_j^p \in \{u, v, w\}$ correspond to the velocity components in the three Cartesian directions. The subscript j is an index identifying individual particles, as multiple particles are tracked in the LPT dataset, and n denotes the total number of tracked particles, t_b represents the time corresponding to each measurement instance for a given particle, where b is the index of the time instance, and there may be up to m time instances per particle.

When constructing the data matrix, it is important to note that, in LPT, the number of detected particle velocities varies across time instances. In LPT, individual particles are tracked throughout the experiment. While some particles remain within the measurement region throughout, others enter the region later and may exit before the experiment concludes [30], as shown in Fig. 4. This inherent characteristic of the technique makes it impossible to maintain a constant particle count throughout the entire experiment. Additionally, at any given time instance, the number of detected particles varies. Figure 5 illustrates two tracked particles that are only available for a portion of the experiment.

4. Methodology

This section describes the proposed approach in this paper for constructing the data matrix and singular value decomposition (SVD) from LPT data for POD analysis. The study utilizes two-dimensional data obtained from real-world experiments conducted under the influence of gravity. Measurements were recorded using a single high-speed camera in a two-dimensional setup.

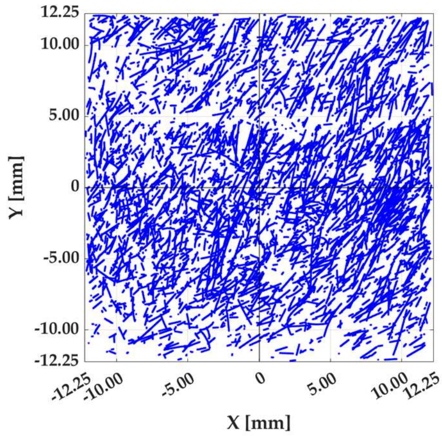

Fig. 4. Tracked particles' motion in the measurement area using the LPT technique for a single experiment.

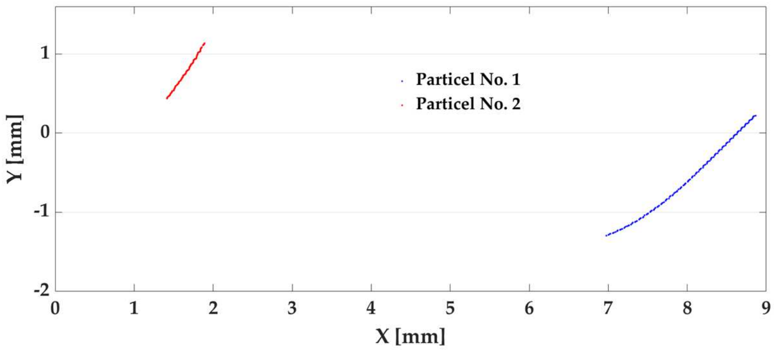

Fig. 5. Displacement of two particles is tracked from the experiment; they can only be observed during a portion of the experiment time.

4.1. Data matrix

In the data matrix used for POD analysis, it is essential to define a matrix $\mathrm{A_{qp}}$, where q denotes the time instant and p denotes the particle velocity at a specific location. In a typical POD setup, the columns of the matrix refer to spatial locations, such as grid points within the problem domain. In standard applications, velocity data is available simultaneously across all domain grid points at each time instant [27]. This framework can be adapted for LPT, where at each time instant, a certain number of particles have specific velocity values at particular locations. The key difference, however, is that in LPT, velocity data is not available for the entire domain at each time instant. Instead, velocity measurements are obtained only from particles within the domain that follow the flow streamlines. Since these are tracer particles, they effectively represent the structure of each streamline within the turbulent flow. Since different LPT setups use varying numbers of cameras, the measurable particle density depends on the specific configuration. Here, the number of tracked particles determines the dimensionality of the modal decomposition.

This approach also aligns with ensemble data analysis in turbulent flow studies, where multiple time instances are used for statistical analysis [3]. In a turbulent flow case, data is collected at different times and used for statistical evaluations [5]. As mentioned in the introduction, due to the inherent perturbations and sensitivity of turbulent flow, even under identical experimental conditions, the data collected in repeated trials will never be exactly the same. Therefore, ensemble analysis relies on data from multiple experiments (realizations) to study turbulent flow behavior and coherent structures. Therefore, in the matrix $\mathrm{A_{qp}}$, each row represents a time instant and contains the velocity data of all detected particles at that moment. Each column corresponds to the velocity vector of an individual particle, which varies throughout the experiment according to the respective time row t. Assuming u as the velocity component in the X-direction, the matrix $\mathrm{A_{qp}}$ is defined as:

$$\mathrm{A_{qp}} = \begin{bmatrix} \mathrm{u_1(t_1)} & \mathrm{u_2(t_1)} & \dots & \mathrm{u}_n\mathrm{(t_1)} \\ \mathrm{u_1(t_2)} & \mathrm{u_2(t_2)} & \dots & \mathrm{u}_n\mathrm{(t_2)} \\ . & . & & . \\ . & . & & . \\ . & . & & . \\ \mathrm{u_1(t}_m) & \mathrm{u_2(t}_m) & \dots & \mathrm{u}_n\mathrm{(t}_m) \end{bmatrix} \tag{7}$$

where n denotes the total number of particles, which corresponds to p, the number of columns in matrix A. Each particle trajectory is recorded over a certain number of temporal instances, denoted by m. Here, a condition is defined that the particle with the minimum tracked point 50 will be kept, and if $m < 50$, that particle is ignored and is not used in matrix A. This setup aligns with the range of the measurement scale of the experiment, which has 10000 *fps*, meaning that the smallest time interval of the captured particle is 0.1 *ms*, which is smaller than the Kolmogorov scale τ_η (35–99 *ms*), and with 50 measurements, it covers at least a 5 *ms* time scale. The maximum number of recorded instances among all particles is defined as $\mathrm{q} = max(m)$.

A data matrix is constructed from p particles, each with at least 50 tracked points, yielding q rows. Based on the matrix dimensions, any row or column containing more than 30% missing (*NaN*) values relative to its length is discarded. This filtering criterion is consistent with the observation that the first 25–30 POD modes typically contain about 70% [31-34] of the total kinetic energy. Consequently, when the number of tracked particles (p) are less than 30, the corresponding matrix is excluded from further analysis, as it is insufficient to extract meaningful modes or accurately represent the energy contribution of the turbulent flow. Moreover, Schiødt et al. [35] demonstrated, through particle POD analysis of single- and multiple-particle realizations, that approximately 8% and 38% of the total modes, respectively, are sufficient to capture 90% of the turbulent flow energy. This requirement holds for realizations with different initial particle separations, spanning from the Kolmogorov to the integral length scales. They also observed that particles starting at smaller separations exhibit stronger velocity correlations, as only the smaller turbulent eddies are capable of driving them apart. In contrast, when the initial particle spacing is larger, the velocity correlation decreases because the particles are influenced by a wider spectrum of turbulent motions. Consequently, particles that are more widely separated experience greater dynamical freedom, leading to a slower convergence rate [35].

For any particle with fewer recorded instances ($m < \mathrm{q}$), the velocity at its final recorded time step is repeated to fill the remaining entries of the corresponding column in A, to construct a uniform data matrix. This procedure ensures consistent dimensionality across all particle data while preserving the final energy state of each particle.

This assumption is consistent with the steady-state condition of HIT [1, 2, 6], in which turbulent kinetic energy is continuously supplied and dissipated at equal rates. Under such conditions, the turbulence statistics remain stationary, and each particle can be considered to maintain its instantaneous velocity (and thus energy level) at the final recorded value. This treatment implies that the particle's energy remains confined to its characteristic scale, without influencing other energy scales within the flow field.

For strained turbulent flows, the applied strain is transient and does not reach a steady-state condition because the strain energy input is momentary and not continuously sustained. Such non-stationary behavior is characteristic of many realistic flow configurations, including homogeneous shear flows and axisymmetric strain fields (e.g., stagnation-point flows) [2, 6, 30].

This modeling assumption is also consistent with experimental observations of tracer particles in stagnation-point regions, such as near the leading edge of an airfoil, where some particles become trapped while others escape the stagnation region. These distinct particle behaviors reflect the localized and non-uniform energy dynamics typical of strained turbulent flows. Since the employed data from two-dimensional experiment, velocity in the X-direction, u and in the Y-direction is v, the matrix rows are duplicated, and the matrix $\mathrm{A}_{2\mathrm{qp}}$ can be reformed as follows:

$$\mathrm{A}_{2\mathrm{qp}} = \begin{bmatrix} u_1(t_1) & u_2(t_1) & \dots & u_n(t_1) \\ u_1(t_2) & u_2(t_2) & \dots & u_n(t_2) \\ \vdots & \vdots & & \vdots \\ u_1(t_m) & u_2(t_m) & \dots & u_n(t_m) \\ v_1(t_1) & v_2(t_1) & \dots & v_n(t_1) \\ v_1(t_2) & v_2(t_2) & \dots & v_n(t_2) \\ \vdots & \vdots & & \vdots \\ v_1(t_m) & v_3(t_m) & \dots & v_n(t_m) \end{bmatrix} \tag{8}$$

In POD analysis, the focus is on examining velocity fluctuations, therefore, the fluctuation is computed as follows [6]:

$$\acute{u} = u - \bar{u} \tag{9}$$

$$\acute{v} = v - \bar{v} \tag{10}$$

where u and v represent the measured (total) velocity, $\acute{u}$ and $\acute{v}$ denote the velocity fluctuations, and $\bar{u}$ and $\bar{v}$ correspond to the mean velocity. Since, in LPT, each particle has its own velocity vector, the fluctuation is computed individually for each particle. For strained turbulent flow, since the condition is unsteady, the mean velocity is computed using ensemble averaging. Specifically, the mean Lagrangian velocity for a given initial position is obtained by averaging the velocity vectors of 20 particles—one selected from each independent experiment—component-wise, as follows:

$$\bar{u} = \frac{1}{\mathit{\Pi}} \sum_{J=1}^{\mathit{\Pi}} u^{(J)} \tag{11}$$

$$\bar{v} = \frac{1}{\mathit{\Pi}} \sum_{J=1}^{\mathit{\Pi}} v^{(J)} \tag{12}$$

here, $\mathit{\Pi}$ is the number of particles, and $u^{(J)}$ and $v^{(J)}$ are the velocity components of the particle from experiment (video) J. Thus, the matrix $\mathrm{A}_{2\mathrm{qp}}$ is reformulated in its final version as follows:

$$\mathrm{A}_{2\mathrm{qp}} = \begin{bmatrix} \acute{u}_1(t_1) & \acute{u}_2(t_1) & \dots & \acute{u}_n(t_1) \\ \acute{u}_1(t_2) & \acute{u}_2(t_2) & \dots & \acute{u}_n(t_2) \\ \vdots & \vdots & & \vdots \\ \acute{u}_1(t_m) & \acute{u}_2(t_m) & \dots & \acute{u}_n(t_m) \\ \acute{v}_1(t_1) & \acute{v}_2(t_1) & \dots & \acute{v}_n(t_1) \\ \acute{v}_1(t_2) & \acute{v}_2(t_2) & \dots & \acute{v}_n(t_1) \\ \vdots & \vdots & & \vdots \\ \acute{v}_1(t_m) & \acute{v}_2(t_m) & \dots & \acute{v}_n(t_m) \end{bmatrix} \tag{13}$$

To define and compute the POD of the defined data in the current study, the SVD is employed.

4.2. Singular value decomposition

The approaches for defining and computing the POD of a given dataset are Singular Value Decomposition (SVD) [36] and eigenvalue decomposition [28]. SVD can be applied to no square matrices, whereas eigenvalue decomposition is strictly defined for square matrices [29]. Additionally, SVD remains within real arithmetic as long as A is real, while the eigenvalues and eigenvectors of non-symmetric real matrices may be complex [28]. Since, in LPT, the number of particles varies, as previously mentioned, the computation involves a non-square matrix. It is important to note that for large datasets, Sirovich [21] proposed the snapshot POD method, which is computationally efficient because the number of snapshots is typically smaller than the number of spatial grid points.

However, in this study, the calculations are based on particle tracking from a Lagrangian viewpoint, rather than working with the entire problem domain grid points. Consequently, SVD will be used to compute POD on all measured particle positions. In snapshot POD, the computation of the POD is based on the number of snapshots rather than the total number of grid points in the domain. Similarly, the approach proposed in this study utilizes data only from tracked points along the flow streamline. Figure 6 presents the two-component velocity measurements (2D) of two particles tracked in the experiment. Sen et al. [37] showed that the 2D POD analysis revealed how surface roughness modifies the size and spacing of the large-scale, energy-containing structures within the flow. The comparison between the proposed approach and Snapshot POD is beyond the scope of this study. Computing SVD of matrix A can define as follows:

$$A = U\Omega C^T \tag{14}$$

here, U is $q \times q$ orthogonal matrix, C is $p \times p$ orthogonal matrix, the superscript T indicates matrix transpose, Ω is $q \times p$ matrix with all elements zero except along the diagonal. The diagonal elements Ω_{ii} consist of $r = min(q, p)$ nonnegative values ω_i, arranged in decreasing order, i.e., $\omega_1 > \omega_2 > \ldots > \omega_r > 0$. The quantities ω are the singular values of A, which are uniquely determined by the matrix. The rank of A corresponds to the number of its nonzero singular values. In the presence of noise, a numerical rank may be introduced, defined as the number of singular values exceeding a prescribed small fraction of the most considerable singular value.

The correspondence between the SVD and the POD can be established by assuming that $U\Omega = \beta$, where β is a matrix of dimensions $q \times p$. Thus, we express A as $A = \beta C^T$. Denoting b_k as the kth column of β and c_k as the kth column of C, the matrix product can be rewritten as follows:

$$A = \beta C^T = \sum_{k=1}^{p} b_k c_k^T \tag{15}$$

Equation (15) represents the discrete form of Eq. (3). Consequently, the function $z(x,t)$ is associated with the matrix A, the function $a_k(t)$ corresponds to the column matrix b_k, and the function $\varphi_k(x)$ is linked to the row matrix c_k. Since the singular values are organized in a specific order, the index k corresponding to the kth singular value is referred to as the singular value number. The eigenvalues of AA^T (or the squares of the singular values of A) are termed "energies," corresponding to the proper orthogonal modes. In incompressible fluid dynamics, when dealing with velocity measurements, this energy is associated with the fluid's kinetic energy [28].

5. Results and Discussion

This section presents and discusses a novel approach to POD analysis from a Lagrangian viewpoint, using data from an LPT method that tracked tracer particles. The data are from experiments that were conducted on HIT and a strained turbulent flow that was initially homogeneous and isotropic. For the strained flow case, the flow underwent strain deformation with a mean strain rate of 8 s^{-1} in the Y-direction (vertical). This paper examines two turbulent flow cases with different Taylor microscale Reynolds numbers: $Re_\lambda \approx 100$ and $Re_\lambda \approx 120$.

5.1. POD analysis for HIT

To investigate the effect of strain deformation on the turbulent energy level and the energy cascade, POD analysis is applied to homogeneous isotropic turbulent (HIT) flows with two levels of turbulent intensity: $Re_\lambda \approx 100$ (Flow-1) and $Re_\lambda \approx 120$ (Flow-2). To assess the energy levels, three realizations of each flow case are examined.

Figure 7(a) shows the results for the three realizations of Flow-1, which is an HIT flow with $Re_\lambda \approx 100$. As mentioned in the introduction and widely reported in the literature [1, 6], even when experimental conditions are maintained, repeating the experiment multiple times can yield slightly different turbulent behavior due to turbulence's sensitivity to initial perturbations [6]. In Fig. 7(a), it can be seen that although the HIT cases share similar conditions, there are slight differences in energy levels.

The mode index in the POD analysis is related to the number of measured data points, as discussed in Section 4. Despite variations in the number of POD modes across realizations, first 25-30 modes cover almost 70% of the turbulent energy [31-34] and the energy spectra exhibit nearly identical slopes and similar energy transfer patterns. However, at a specific mode index, the energy spectrum curve shows a turning point where the slope changes and the decay becomes steeper. Prior to this inflection point, the dominant coherent structures are responsible for carrying the majority of the turbulent kinetic energy. Beyond this point, the flow structures likely transition to smaller scales that contribute less significantly to the total energy. This behavior will be further discussed in the subsection on turbulent energy contribution results.

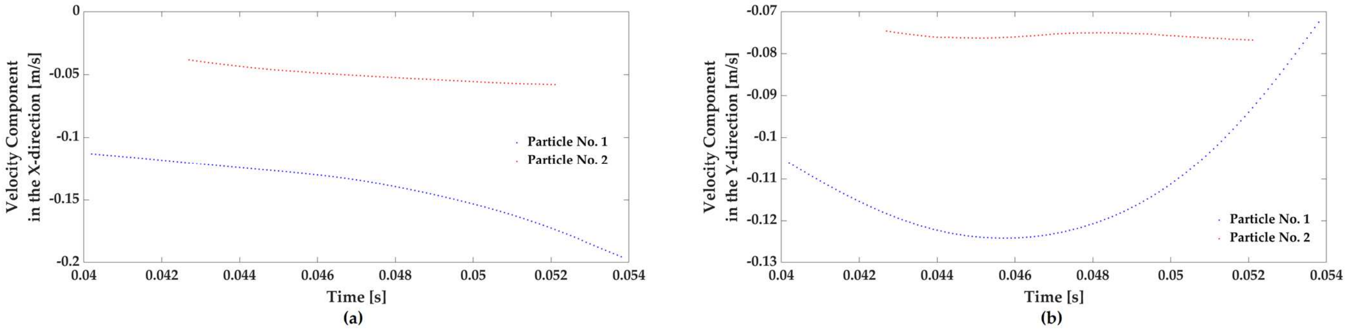

Fig. 6. Velocity components of two particles tracked using LPT in a turbulent flow: (a) velocity component in the X-direction, (b) velocity component in the Y-direction.

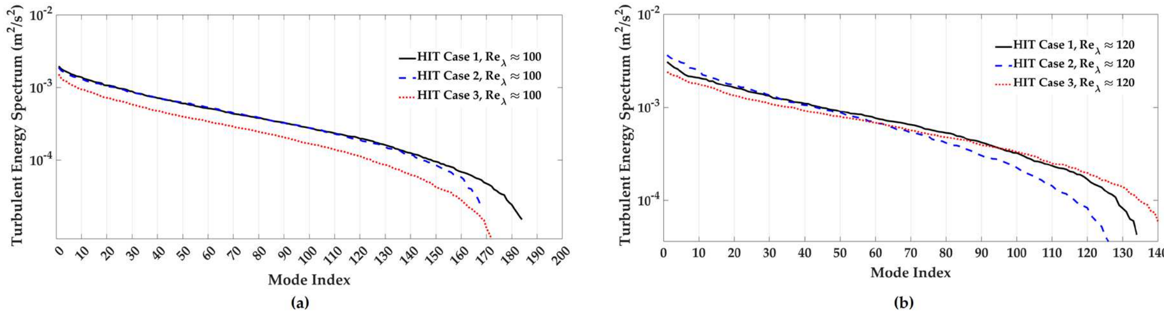

Fig. 7. Turbulent energy spectrum for hematogenous isotropic turbulent (HIT) flow by POD analysis, for three cases with similar experiment setup: (a) $Re_\lambda \approx 100$ and (b) $Re_\lambda \approx 120$.

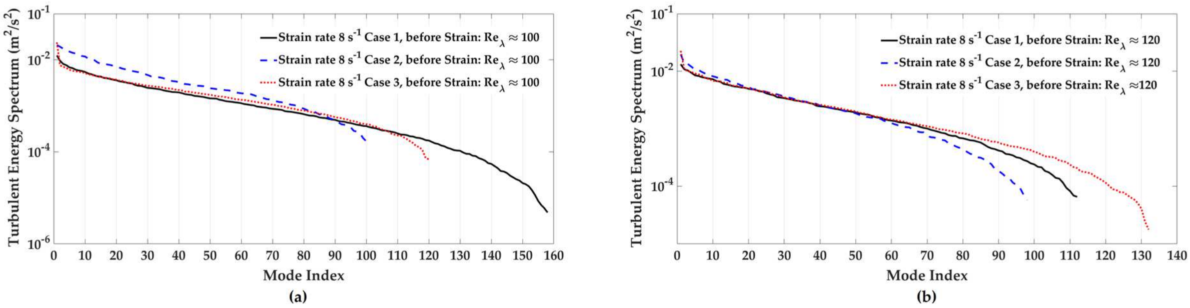

Fig. 8. Turbulent energy spectrum for strained turbulent flow by POD analysis, for three cases with similar conditions before the strain deformation: (a) $Re_\lambda \approx 100$ and (b) $Re_\lambda \approx 120$.

Flow-2, with a higher turbulence intensity ($Re_\lambda \approx 120$), is shown in Fig. 7(b) and is based on three realizations. While the overall energy levels show slight variations across cases, the energy spectra again exhibit consistent slopes and similar energy-transfer behavior. A turning point is also evident in these realizations. These results indicate that experiments conducted under the same conditions produce flow realizations with consistent energy cascades and transfer rates, which may extend to the dissipation range. Furthermore, the initial energy levels of the different realizations are nearly the same, and they converge to approximately the same final energy level. Although each realization may follow a slightly different trajectory, they start and end at comparable energy states. It is important to note that this analysis is based on the inertial subrange of the energy cascade, which reflects a universal equilibrium regime, as noted in the experiment's original work [1].

5.2. POD analysis for strained turbulent flow

The POD analysis is applied to strained turbulent flows with a mean strain rate of 8 s^{-1} in the Y-direction. Two cases are studied: Flow-3 and Flow-4, which had initial conditions of $Re_\lambda \approx 100$ and $Re_\lambda \approx 120$, respectively. Both flows are initially homogeneous and isotropic before strain is applied. The correlation of Reynolds stress anisotropy with strain is well documented in the literature [3, 6], and the present experimental data support this, as shown in Fig. 2.

Figure 8(a) presents three realizations of the strained turbulent Flow-3. Across a specific range of modes, the energy spectra share a similar slope. At a particular mode index, a turning point is observed, after which the spectrum exhibits a steeper decline. Additionally, the final energy levels at the end of the spectrum differ slightly across realizations, partly due to differences in the number of available modes. It is important to note, however, that in HIT realizations, the energy spectra tend to converge toward a similar endpoint, even when the number of modes differs. For Flow-3, all three realizations start from approximately the same energy level and follow closely aligned curves, with only slight variations at specific points.

Figure 8(b) shows three realizations of Flow-4, which has a higher turbulence intensity than Flow-3. Despite the increased intensity, the realizations exhibit similar behavior and follow the same energy-spectrum pattern described for Flow-3. Figures 8(a) and 8(b) demonstrate that different realizations of strained turbulent flow under similar conditions exhibit consistent energy-spectrum slopes before the turning point and maintain comparable energy levels. However, the endpoints of the energy spectra vary between realizations. This divergence may be attributed to the influence of small-scale structures beyond the turning point, where viscous effects become dominant and may impact the energy spectrum.

5.3. Turbulent energy contribution in POD

The POD analysis of the velocity fluctuation data matrix provides the energy contribution associated with each calculated mode. Since the mode index corresponds to the energy spectrum of coherent structures in turbulent flow, the energy associated with each mode highlights the dominant structures that shape and strongly affect the turbulent flow dynamics. Table 1 presents the energy contributions of the first ten modes for the flow cases considered in the current study. Usually, the first few modes make the most significant energy contribution in turbulent flow [28]; however, this contribution can vary with flow conditions. According to Table 1, for HIT flow with different turbulence intensities, the first ten modes exhibit a similar pattern, with only slight differences that can be attributed to the higher turbulence intensity.

In the case of strained turbulent flow, which initially started as homogeneous isotropic turbulence and subsequently underwent strain deformation, the energy contributions of the first few modes increased significantly, by factors of 2 or even 3. Table 1 reveals that a portion of the flow's energy was transferred to the first few modes, which then shared this energy and exhibited notably higher contributions. This observation demonstrates that strain deformation not only increases the overall energy level of the energy spectrum but also enhances the energy contribution of the dominant structures within the turbulent flow. All computations are carried out on a workstation with an 11th Gen Intel® Core™ i7-1185G7 CPU (4 cores, 8 threads, 3.0–4.8 GHz) and 32 GB RAM using MATLAB. Each realization of the POD-LPT analysis here is required about 30–50 seconds, depending on the size of the matrix A_{qp}.

Table 1. Turbulent energy contribution corresponding to each mode of POD analysis for Lagrangian viewpoint data.

	Energy Contribution %			
Mode Index	HIT, $Re_\lambda \approx 100$	HIT, $Re_\lambda \approx 120$	Strain 8 s^{-1}, $Re_\lambda \approx 100$	Strain 8 s^{-1}, $Re_\lambda \approx 120$
1	2.35	2.39	5.37	7.34
2	2.15	2.27	4.13	3.54
3	2.06	2.19	3.51	3.22
4	1.98	2.15	3.30	3.14
5	1.91	2.04	2.96	2.96
6	1.82	1.96	2.85	2.86
7	1.78	1.87	2.63	2.71
8	1.71	1.82	2.53	2.42
9	1.69	1.81	2.47	2.38
10	1.66	1.76	2.35	2.21

5.4. Turbulent energy spectrum

Figure 9 presents a comparison of realizations from four different turbulent flows: HIT with $Re_\lambda \approx 100$, HIT with $Re_\lambda \approx 120$, strained flow with a mean strain rate of 8 s^{-1} (initially $Re_\lambda \approx 100$), and strained flow with the same strain rate but with initial $Re_\lambda \approx 120$.

Comparing the two HIT realizations with different turbulence intensities reveals that the flow with the higher Reynolds number ($Re_\lambda \approx 120$) exhibits a higher energy level across the spectrum. This result is consistent with the understanding that flows with higher turbulence intensity tend to maintain higher energy levels.

A similar trend is observed for the strained turbulent flows. Despite having the same applied strain rate, the flow that starts with a higher Reynolds number maintains a higher turbulent energy level throughout the spectrum.

Furthermore, when comparing HIT and strained realizations at the same initial Reynolds number ($Re_\lambda \approx 100$), it is evident that the flow subjected to strain exhibits a higher spectral energy level. This aligns with findings in the literature suggesting that strain enhances velocity fluctuations in turbulent fields [3], thereby increasing turbulent energy. A comparable behavior is also observed for the flows with $Re_\lambda \approx 120$.

Additionally, all realizations exhibit a turning point at approximately the same mode index range. This turning point typically occurs where 85%–95% of the total turbulent energy is captured by the dominant modes. It appears to mark a transition in the energy spectrum, beyond which small-scale structures become dominant, leading to a steeper slope. This suggests that the turning point may mark a critical scale at which viscous effects begin to influence the energy cascade.

As previously mentioned regarding the energy contributions of the corresponding modes, although strain increases the overall energy level of the spectrum, all flow cases eventually approach a turning point at which their energy levels become approximately equal. This suggests that beyond this point, all flows converge toward a similar level of turbulent flow structure and energy, which may be associated with small-scale features.

Moreover, the slope of the energy spectrum in the limited range preceding the turning point is approximately –5/3 for HIT realizations and approximately –7/3 for the strained flow. For HIT flow, based on the Kolmogorov power law [2, 6], the energy spectrum exhibits a –5/3 scaling from large to small scales within the inertial subrange, both in frequency and wavenumber space. The POD analysis conducted in the current study also reveals a power-law energy spectrum, with a correlation and similarity based on mode analysis. The calculated power-law scaling for the energy spectrum versus mode number in HIT flow is approximately –5/3.

Furthermore, the calculations show that strained turbulent flows with different initial turbulence intensities, specifically $Re_\lambda \approx 100$ and $Re_\lambda \approx 120$, exhibit a similar power-law scaling of approximately –7/3. These observations indicate that, although the strained turbulent flow has a higher overall energy level than the HIT flow, it still exhibits a power-law relationship between the energy spectrum and the mode number. The present findings are consistent with the shear-stress spectrum, wherein the mean strain rate induces anisotropy in the turbulent field. Lumley [6,38] demonstrated that the energy cascade follows a –7/3 slope under strain distortion. The modes within the energy-containing range decay more rapidly than predicted under conditions of local isotropy. Moreover, Hodzic et al. [39] reported that the –7/3 range in the cross-spectra can be fully reconstructed using a single mode in regions of high mean shear, and that shear stresses are almost entirely reconstructed using the first two modes. These observations indicate that the primary contribution to energy production associated with shear stresses originates from the first POD mode [39].

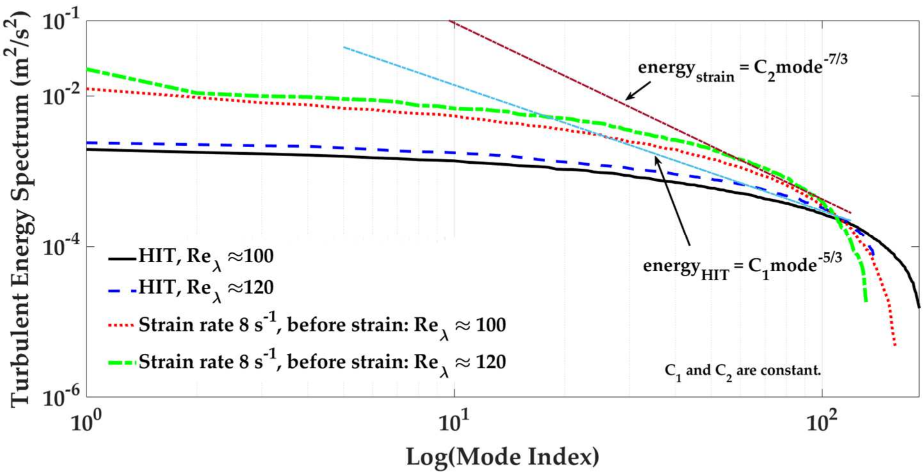

Fig. 9. Turbulent energy spectrum comparison: black color line is HIT, $Re_\lambda \approx 100$, dashed blue color line is HIT, $Re_\lambda \approx 120$, dashed red color line is strained turbulent flow, before strain had $Re_\lambda \approx 100$, dashed green color line is strained turbulent flow, before strain had $Re_\lambda \approx 120$. Blue line (slope = –5/3): trend for HIT flow cases; Red line (slope = –7/3): trend for strained turbulent flow cases.

6. Conclusion

This paper presented the application of Proper Orthogonal Decomposition (POD) analysis on experimental data obtained from a Lagrangian perspective in a 2D setup using a single high-speed camera. The experimental dataset was sourced from an experimental study [1], with full details available in the original publication. Two flow conditions were analyzed: Homogeneous Isotropic Turbulence (HIT) and strained turbulent flow which was initially homogeneous isotropic. Each condition included two cases with different turbulence intensities, characterized by $Re_\lambda \approx 100$ and $Re_\lambda \approx 120$. The data matrix was constructed from Lagrangian Particle Tracking (LPT) measurements, which record the velocity components of individual particles. This approach significantly reduces computational cost compared to traditional POD, which requires full-domain velocity fields. In essence, the LPT-POD method captures flow characteristics by following the motion of tracer particles along turbulent flow streamlines, rather than relying on data from a fixed grid. POD analysis was applied to both HIT and strained turbulent flows to investigate the energy spectrum in the presence of strain. The results indicated that, for the HIT case, a few dominant POD modes capture a substantial portion of the total energy, corresponding to coherent flow structures. When external strain was introduced, the overall energy levels in the spectrum increased, with an even larger portion of energy concentrated in the dominant modes—up to two or three times more than in the unstrained case. For HIT flows with varying turbulence intensities, POD analysis showed that higher Re_λ corresponds to higher overall energy levels, while the energy-spectrum slope remains consistent across cases. This slope follows the -5/3 power law, which has similarity with Kolmogorov's theory in both frequency and wavenumber domains [2, 6]. In the strained turbulence flow, higher turbulence intensity also resulted in a higher energy spectrum. However, both strained flow cases shared the same spectral slope of approximately –7/3, indicating that a distinct power-law behavior is preserved and observable in the POD analysis and consistent with the shear-stress power law by Lumley [6, 38]. Across all flow cases, the energy spectrum curves exhibited a turning point at a similar mode index range. Before this point, approximately 85%–95% of the total energy was captured by the corresponding dominant turbulent structures. Beyond this point, the spectrum slope became sharply negative, likely corresponding to smaller-scale structures where viscous effects dominate. The dominant flow structures associated with the highest energy modes—typically the first few mode indices—can be effectively used for Lagrangian velocity reconstruction. These modes are particularly relevant for ML and DL applications, especially in the context of dimensionality reduction techniques.

Author Contributions

R. Hassanian contributed to the conceptualization, method, software, data analysis, visualization, and writing—original draft preparation.

Acknowledgments

The author would like to express his sincere gratitude to Prof. Morris Riedel (University of Iceland) for his many valuable suggestions, which have been incorporated into the manuscript. The author also wishes to thank Prof. Ármann Gylfason (Reykjavik University) and Prof. Chung-Min Lee (California State University, Long Beach, USA) for their insightful technical comments regarding the experimental data.

Conflict of Interest

The author has no conflicts to disclose.

Funding

Not applicable.

Data Availability Statements

The data that support the findings of this study are available from the corresponding author upon reasonable request.

References

[1] Hassanian, R., Helgadottir, A., Bouhlali, L., Riedel, M., An experiment generates a specified mean strained rate turbulent flow: Dynamics of particles, *Physics of Fluids*, 35(1), 2023, 015124.
[2] Tennekes, H., Lumley, J. L., *A First Course in Turbulence*, MIT Press, Massachusetts, 1972.
[3] Davidson, P. A., *Turbulence: An Introduction for Scientists and Engineers*, Oxford University Press, London, 2004.
[4] Berkooz, G, Holmes, P., Lumley, J. L., The proper orthogonal decomposition in the analysis of turbulent flows, *Annual Review of Fluid Mechanics*, 25, 1993, 539.
[5] Batchelor, G. K., *The Theory of Homogeneous Turbulence*, Cambridge University Press, London, 1982.
[6] Pope, S. B., *Turbulent Flows*, Cambridge University Press, London, 2000.
[7] Jackson, D., Launder, B., Osborne Reynolds and the publication of his papers on turbulent flow, *Annual Review of Fluid Mechanics*, 39, 2007, 19.
[8] Versteeg, V., *An Introduction to Computational Fluid Dynamics*, Pearson Education, London, 2007.
[9] Courant, R., Friedrichs, K., Lewy, H., Über die partiellen differenzengleichungen der mathematischen physik, *Mathematische Annalen*, 100, 1928, 32.
[10] Thom A., Taylor, G. I., The flow past circular cylinders at low speeds, *Proceedings of the Royal Society of London. Series A, Containing Papers of a Mathematical and Physical Character*, 141(845), 1993, 651.
[11] Hassanian, R., Myneni, H., Helgadottir, A., Riedel, M. Deciphering the dynamics of distorted turbulent flows: Lagrangian particle tracking and chaos prediction through transformer-based deep learning models, *Physics of Fluids*, 35(7), 2023, 075118.
[12] Hassanian, R., Aach, M., Lintermann, A., Helgadóttir, A., Riedel, M., Turbulent flow prediction-simulation: Strained flow with initial isotropic condition using a GRU model trained by an experimental Lagrangian framework, with emphasis on hyperparameter optimization, *Fluids*, 9(4), 2024, 84.
[13] Sathyanarayana, S., Bernardini, M., Modesti, D., Pirozzoli, S., Salvadore, F., High-speed turbulent flows towards the exascale: Streams-2 porting and performance, *Journal of Parallel and Distributed Computing*, 196, 2025, 104993.
[14] Hassanian, R., Helgadottir, A., Riedel, M., Deep learning forecasts a strained turbulent flow velocity field in temporal Lagrangian framework: Comparison of LSTM and GRU, *Fluids*, 7(11), 2022, 344.
[15] Hassanian, R., Helgadóttir, A., Gharibi, F., Beck, A., Riedel, M., Data-driven deep learning models in particle-laden turbulent flow, *Physics of Fluids*, 37(2), 2025, 023348.
[16] Hassanian, R., Riedel, M., Bouhlali, L., The capability of recurrent neural networks to predict turbulence flow via spatiotemporal features, *In 10th*

IEEE Jubilee International Conference on Computational Cybernetics and Cyber-Medical Systems (ICCC), 2022, 000335–000338.
[17] Olesen, P. J., Hodžic, A., Andersen, S. J., Sørensen, N. N., Velte, S. M., Dissipation optimized proper orthogonal decomposition, *Physics of Fluids*, 35(1), 2023, 015131.
[18] Olesen, P. J., Soucasse, L., Podvin, B., Velte, C. M., Dissipation-based proper orthogonal decomposition of turbulent Rayleigh–Bénard convection flow, *Physics of Fluids*, 36(3), 2024, 035109.
[19] Hang, Y., Hodžic, A., Evrard, F., van Wachem, B., Velte, C. M., Phase proper orthogonal decomposition of non-stationary turbulent flow, *Physics of Fluids*, 35(4), 2023, 045109.
[20] Rovira, M., Engvall, K., Duwig, C., Proper orthogonal decomposition analysis of the large-scale dynamics of a round turbulent jet in counterflow, *Physical Review Fluids*, 6(1), 2021, 014701
[21] Sirovich, L., Turbulence and the dynamics of coherent structures. Part I: Coherent structures, *Quarterly of Applied Mathematics*, 45(3), 1987, 561.
[22] Podvina, B., Fraigneau, Y., A few thoughts on proper orthogonal decomposition in turbulence, *Physics of Fluids*, 29(2), 2017, 020709.
[23] Ouellette, N. T., Xu, H., Bodenschatz, E., A quantitative study of three-dimensional Lagrangian particle tracking algorithms, *Experiments in Fluids*, 40(2), 2006, 301.
[24] Kosambi, D. D., *Statistics in Function Space*, Springer India, New Delhi, 2016.
[25] Narasimha, R., Kosambi and proper orthogonal decomposition, *Resonance*, 16(6), 2011, 574.
[26] Borra, A., Flynn, Z., Goza, A., Saxton-Fox, T., Intrinsic phase-based proper orthogonal decomposition (iphab pod): a method for physically interpretable modes in near-periodic systems, *Journal of Fluid Mechanics*, 1002, 2025, A18.
[27] Dawson, S., *The Proper Orthogonal Decomposition*, Cambridge University Press, 2023.
[28] Chatterjee, A., An introduction to the proper orthogonal decomposition, *Current Science*, 78(7), 2000, 808.
[29] Weiss, J., A tutorial on the proper orthogonal decomposition, *In 2019 AIAA Aviation Forum*, 17–21 June, Dallas, Texas, United States, American Institute of Aeronautics and Astronautics, 2019
[30] Hassanian, R., Riedel, M., Leading-edge erosion and floating particles: Stagnation point simulation in particle-laden turbulent flow via Lagrangian particle tracking, *Machines*, 11(5), 2023, 566.
[31] Sirovich, L., Ball, K. S., Keefe, L. R., Plane waves and structures in turbulent channel flow, *Physics of Fluids*, 2(12), 1990, 2217–2226.
[32] Moin, P., Moser, R. D., Characteristic-eddy decomposition of turbulence in a channel, *Journal of Fluid Mechanics*, 200, 1989, 471–509.
[33] Ball, K. S., Sirovich, L., Keefe, L. R., Dynamical eigenfunction decomposition of turbulent channel flow, *International Journal for Numerical Methods in Fluids*, 12, 1991, 585–604.
[34] Osman, H., Wang, W., Ikegaya, N., POD dimensional reduction for preserving turbulence statistics in urban environment, *Building and Environment*, 287, 2026, 113927.
[35] Schiødt, M., Hodžic, A., Evrard, F., Hausmann, M., Van Wachem, B., Velte, C. M., Characterizing Lagrangian particle dynamics in decaying homogeneous isotropic turbulence using proper orthogonal decomposition, *Physics of Fluids*, 34(6), 2022, 063303.
[36] Stewart, G. W., On the early history of the singular value decomposition, *SIAM Review*, 35, 1993, 551.
[37] SEN, M., Bhaganagar, K., Juttijudata, V., Application of proper orthogonal decomposition (POD) to investigate a turbulent boundary layer in a channel with rough walls, *Journal of Turbulence*, 8, 2007, https://doi.org/10.1080/14685240701615960.
[38] Lumely, J. L., Similarity and the turbulent energy spectrum, *Physics of Fluids*, 10, 1967a, 855-858.
[39] Hodžic, A., Meyer, K. E., George, W. K., Velte, C. M., Lumley Decomposition of the Turbulent Round Jet Far-field. Part 2 – Dynamics, arXiv preprint arXiv:1909.01307, 2019.

ORCID iD

Reza Hassanian https://orcid.org/0000-0001-5706-314X

How to cite this article: Hassanian R. Proper Orthogonal Decomposition Analysis of Turbulent Energy Spectra within a Lagrangian Particle Tracking Framework, *J. Appl. Comput. Mech.*, xx(x), 2025, 1–11.
https://doi.org/10.22055/jacm.2025.48733.5459